
COMPLEX SYSTEMS
BIOPHYSICS

Model with Asymptotically Stable Dynamics for *Drosophila* Gap Gene Network

V. V. Gursky^a, K. N. Kozlov^b, A. M. Samsonov^a, and J. Reinitz^c

^a Ioffe Physico-Technical Institute, Russian Academy of Sciences, St. Petersburg, 194021 Russia

^b St. Petersburg State Polytechnic University, St. Petersburg, 195251 Russia

^c Stony Brook University, Stony Brook, NY 11794–3600, USA

e-mail: gursky@math.ioffe.ru

Received August 20, 2007

Abstract—We consider a model of gap gene expression during the early development of *Drosophila* embryo. Parameter values in the model have been obtained by fitting to experimental patterns under an additional condition that the solution be asymptotically stable at large times. The patterns at the beginning of gastrulation in such solutions are very close to an actual attractor in the model. It is shown that such solutions are more robust to perturbations of concentrations and parameter values in the model.

Key words: mathematical model, segmentation gene expression, attractors, model robustness

DOI: 10.1134/S0006350908020085

INTRODUCTION

This is a study of a mathematical model describing the spatiotemporal dynamics of gap gene expression patterns in the fruit fly *Drosophila melanogaster*. The gap gene system is one of the four in the system of segmentation genes in *Drosophila*. The segmentation gene expression determines the morphology of repeating units of the fly body called segments [1, 2].

Segment determination takes place at the embryo development stage from about the 10th nuclear cleavage cycle to the end of 14 A. The whole embryo in this period is one big cell with many nuclei inside (syncytial blastoderm). The cell membranes begin to grow around nuclei only in the middle of cycle 14 A. The segmentation gene system includes maternal coordinate genes, gap genes, pair-rule genes, and segment-polarity genes [3, 4]. The spatial gradients of morphogen protein concentrations coded by maternal coordinate genes *bicoid* (*bcd*), *hunchback* (*hb*), and *caudal* (*cad*) provide the initial conditions for cell fate determination along the anteroposterior (A–P) axis of the embryo. The other three classes of the segmentation system consist of zygotic genes. In the course of development, the gap and pair-rule gene expression patterns control the patterns for segment-polarity gene family, whose most important constituents are genes *wingless* and *engrailed*. The first transcripts of these genes appear late in 14 A. These genes are the last element determining the pre-pattern of the final segmentation [3, 4].

There are several models of the gap gene network [5–9]. Here we develop a model [9, 10] that in our opinion currently provides the best spatiotemporal approximation of the experimental data. One of the problems

found in the model is that solutions prove not very stable against perturbations of initial conditions and parameter values. The parameter values in the model are found by fitting the solution to experimental expression patterns at the time interval $0 \leq t \leq \tau$ covering cleavage cycles 13 and 14 A, which is about 71 min. It turns out that at these parameter values the solution holds at time $t = \tau$, corresponding to the end of cycle 14 A and start of gastrulation, but changes its shape significantly if one continues integrations at $t > \tau$. In other words, solutions at the beginning of gastrulation are far from the actual attractors in the model, where attractors mean the limit states of solutions at large times $t \gg \tau$ (they are stationary patterns in the model). Following the dynamical systems theory, it is reasonable to suppose that robustness could be improved in the reverse situation, in which solutions at $t = \tau$, which are the final patterns for the biologically important time period, would not essentially change at $t > \tau$, i.e., be asymptotically stable at large times and, therefore, close to the attractors in the model.

To check this idea, we have modified the model by applying an additional restriction for solutions to be asymptotically stable at large times. We have found three sets of parameter values providing good fit. The stability of solutions in these three models has been compared to that in seven variants of the initial model [9, 10].

The solution stability in mathematical models of various biological systems in the general context determines the property known as robustness of the system. The latter can be defined as the ability of the system to maintain a certain “function” under noisy conditions of

various nature [11]. Two types of noise sources are usually recognized. The external noise is determined by factors of the external medium. The internal noise is associated with the basic variability of the mechanisms underlying the system function. At the level of model equations, the external noise is expressed through perturbations of parameter values. The influence of internal noise can be modeled by stochastic perturbations of solutions at various time moments, since, strictly speaking, protein concentrations are not deterministic functions of time.

We study the stability of the gap gene expression model under perturbations of both types, trying to maximally approach the noise estimates from experimental data in a mathematical description of the perturbations.

THE MODEL

Equations

We model the expression in a gene network consisting of zygotic gap genes *hb*, *Krüppel* (*Kr*), *giant* (*gt*), *knirps* (*kni*), *tailless* (*tll*), and *cad*. Because the expression patterns for these genes are almost constant along the dorsoventral axis of the embryo, we consider a line of nuclei along the A–P axis. The patterns are functions of a unidimensional spatial variable along this axis. We study the gene expression in a spatial domain from 35 to 92% of the A–P axis length.

The internal state of the *i*-th nucleus at moment *t* is determined by the set of concentrations $v_i^a(t)$ of proteins encoded by genes with indices *a*. The concentration dynamics depends on the rates of three processes: protein synthesis, diffusion, and breakdown. These processes are described by the sum of three terms in the right-hand side of the model equations [5, 9, 12]:

$$\frac{dv_i^a}{dt} = \chi(t)R^a g \left(\sum_{b=1}^N T^{ab} v_i^b + m^a v_i^{Bcd} + h^a \right) + D^a(n)[\delta_i^1(v_{i-1}^a - v_i^a) + \delta_i^M(v_{i+1}^a - v_i^a)] - \lambda^a v_i^a, \quad (1)$$

where $a = 1, \dots, N$, $N = 6$ is the total number of genes in the network; $i = 1, \dots, M$, $M = M(n)$ is the number of nuclei that changes in time by nuclear divisions in the system, *n* is the current number of the cleavage cycle. The coefficient R^a defines the maximal possible protein synthesis rate for gene *a*, and D^a and λ^a are diffusion and degradation constants, respectively. The parameters T^{ab} characterize the regulatory action on gene *a* protein synthesis by the protein of gene *b*. The quantity v_i^{Bcd} describes the time-constant concentration of maternal protein Bcd in nucleus *i*. The relative rate of *a*-th protein synthesis is quantitated by the sigmoid function *g* of the form

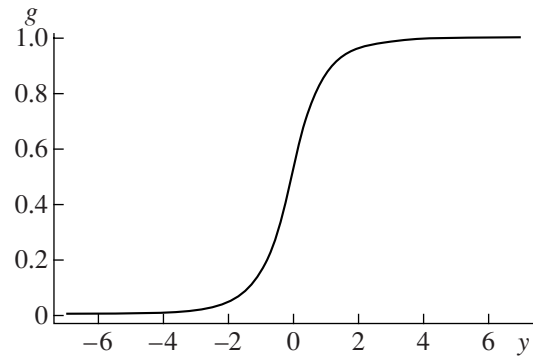


Fig. 1. The graph of $g(y)$.

$$g(y) = \frac{1}{2} \left(1 + \frac{y}{\sqrt{1+y^2}} \right).$$

The graph of $g(y)$ is shown in Fig. 1. The argument of *g* in Eqs. (1) describes the sum of all inputs to regulation of *a*-th protein synthesis. The starting point in time is at the beginning of cleavage cycle 13, and solutions are biologically meaningful until the end of cycle 14 A. This period consists of the following parts: $0 \leq t < 16$ min is the interphase period in cycle 13; $16 \leq t < 21.1$ min is the mitosis period in cycle 13; and $21.1 \leq t \leq \tau = 71.1$ min is the interphase in cycle 14 A. The function $\chi(t)$ models the mitosis at the end of cycle 13. Namely, $\chi(t) \equiv 1$ during the interphase, and $\chi(t) \equiv 0$ during the mitosis, accounting for the fact that protein synthesis shuts down for this time.

The number of nuclei $M(n)$ is constant during each cycle and doubles at the transition from cycle 13 to 14 A owing to nuclei cleavage. We take $M = 30$ in cycle 13 ($t < 21.1$ min) and $M = 58$ in 14 A ($t \geq 21.1$ min; after the division of two boundary nuclei, two of the four daughter nuclei are excluded from the model as leaving the spatial domain). The coefficients δ_i^1 and δ_i^M in the diffusion term account for the boundary nuclei effect. We have $\delta_i^1 = 0$ for $i = 1$, which means that diffusion from the first nucleus occurs only to the second one, and $\delta_i^1 = 1$ otherwise. The multiplier δ_i^M similarly discriminates the nucleus $i = M$. The diffusion coefficient $D^a(n)$ depends on the cycle number *n* as $D^a(n) = 4D^a(n - 1)$. The formula follows from the assumption that the diffusion coefficient is inversely proportional to the squared distance between neighboring nuclei, and this distance is halved after each division.

The initial conditions for Eqs. (1) are as follows. The initial values $v_i^{Cad}(0)$ and $v_i^{Hb}(0)$ in each nucleus equal the concentrations of maternal proteins Cad and Hb, respectively. For all other genes, $v_i^a(0) = 0$.

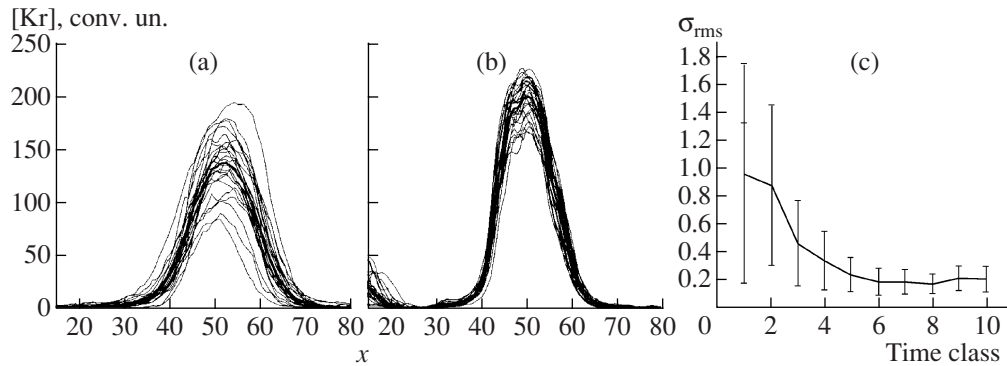


Fig. 2. The canalization effect for the experimental individual curves of gap gene protein concentrations during the early development of *Drosophila* embryo. The effect is demonstrated for the Kr protein. Panels (a) and (b) show the individual (grey curves) and the all-embryos-averaged Kr concentrations (black curves) at time classes (a) T2 and (b) T8. The spatial coordinate along the abscissa is the percentage of the A–P axis length. Panel (c) presents the embryos-averaged σ_{rms} from (3) for Kr and the standard deviation (error bars) as functions of time class. The Ω domain in (3) is the 40–60% range of the A–P axis, which is the *Kr* expression domain. The time classes include one moment each in cycles 12 and 13 and eight moments (T1–T8) in 14 A, numerated from 1 to 10 in this order. All experimental data are from FlyEx [14]. The samples of embryos with measured Kr protein concentration contain 8 embryos in cycle 12 and 21–46 in cycle 13 and at T1–T8. The processing procedure for the experimental data in time classes 1–3 differs from that in classes 4–10 [14]. Panels (a) and (b) are adapted from [16, 18].

Optimization of Parameters under Requirement of Asymptotic Stability

None of the parameters (R^a , D^a , λ^a , T^{ab} , m^a , h^a) in model (1) are known a priori, and their values can be found by fitting the solution to experimental data. This has been done before [9]; in contrast, our aim here was to find parameter values that would provide a solution close to experimental patterns at the time interval $0 \leq t \leq \tau$ and make the solution at $t = \tau$ almost stationary at times $t > \tau$ (i.e. make the solution at the gastrulation stage close to the actual attractor).

One should emphasize that model (1) has no biological sense at times $t > \tau$, because new complex processes start after the beginning of gastrulation, but these are not taken into account in the equations. We should consider the solution behavior at these times as artificial, and the control of this behavior is completely in our hands unless it affects the correct dynamics in the $0 \leq t \leq \tau$ period. Therefore, the biological meaning of this optimization problem is not in trying to model the expression patterns at times $t > \tau$. The goal is to improve the stability of solutions at $t \leq \tau$ by choosing the best description at $t > \tau$.

The optimization procedure should minimize the functional

$$F = \sqrt{\frac{1}{L} \sum_{a,i,k} (\nabla_i^a(t_k)_{\text{model}} - \nabla_i^a(t_k)_{\text{data}})^2} \quad (2)$$

where the difference is taken between the model and the experimental concentrations in each nucleus. The summation is performed over all genes, nuclei, and K time moments t_k for which the data exist. The overall number of terms in (2) is denoted as L . The experimental data are the integrated expression patterns for each gene from the FlyEx database [13, 14]. The integrated

patterns are average expression profiles across many embryos. The data at the interval $0 \leq t \leq \tau$ are used at one moment in cleavage cycle 13 and eight moments in 14 A. To provide asymptotic stability of the solution from $t = \tau$ at large times, additional “artificial” data are used in functional (2), obtained by copying data from $t = \tau$ to seven moments in the interval $100 \leq t \leq 2000$ min. Therefore, we have $K = 16$. The optimization has been done by the simulated annealing method modified for parallel calculations [5, 15].

Rationale for Using Attractors Based on Experimental Data Analysis

We use the requirement for solutions at gastrulation to be close to attractors only to increase the solution stability. The validity of this requirement can be proved or disproved only by the quality of modeling results. However, we believe that the analysis of experimental data supports the hypothesis of quasistationarity for expression patterns setting in at the end of cycle 14 A.

Using experimental gap gene expression patterns from FlyEx, obtained by staining embryos with fluorescent antibodies and subsequent scanning confocal microscopy [14], we investigated the variation of experimental protein concentration functions in different embryos, called “individual” concentration curves, around the all-embryos-averaged functions at various times. The data were available for ten moments, called time classes: cleavage cycles 12 and 13 and eight moments T1–T8 in 14 A. As an example, Figs. 2a, 2b show the spread of individual concentration curves for the Kr protein around the averaged concentration curve at T2 and T8. One can see that the embryo-to-embryo variability at earlier times is much larger than at T8, which is close to the onset of gastrulation.

Table 1. Parameter values in models A_1 – A_3

	T^{ab}							R^a	D^a	λ^a	m^a	h^a
	<i>cad</i>	<i>hb</i>	<i>Kr</i>	<i>gt</i>	<i>kni</i>	<i>tll</i>						
<i>cad</i>	-0.082	-0.054	-0.023	-0.025	-0.020	0.005	A_1	14.955	0.056	0.044	0.001	10.666
	-0.036	-0.019	-0.001	-0.018	-0.013	-0.025	A_2	14.996	0.198	0.039	-0.264	7.028
	-0.088	-0.036	-0.036	-0.053	-0.031	-0.043	A_3	14.993	0.198	0.040	-0.188	15.335
<i>hb</i>	-0.002	-0.010	-0.014	-0.015	-0.190	-0.019	A_1	14.985	0.179	0.069	0.053	2.371
	-0.007	-0.018	-0.029	-0.039	-0.145	-0.024	A_2	15.000	0.199	0.072	0.123	3.823
	0.030	0.001	-0.001	-0.007	-0.114	-0.002	A_3	14.961	0.016	0.053	0.104	-3.500
<i>Kr</i>	0.063	-0.024	0.036	-0.051	-0.031	-0.193	A_1	12.258	0.200	0.063	0.137	-5.153
	-0.082	-0.044	-0.019	-0.139	-0.037	-0.053	A_2	15.000	0.200	0.068	-0.177	15.075
	0.090	-0.004	0.057	-0.104	-0.023	-0.017	A_3	10.278	0.200	0.051	0.150	-11.301
<i>gt</i>	0.045	-0.017	-0.128	0.001	-0.010	-0.028	A_1	14.955	0.127	0.068	0.184	-3.909
	0.085	0.025	-0.030	0.041	0.021	-0.020	A_2	14.950	0.120	0.086	0.179	-13.813
	0.037	0.031	-0.117	0.018	-0.001	-0.018	A_3	14.984	0.138	0.078	-0.060	-3.500
<i>kni</i>	0.044	-0.014	-0.026	-0.047	0.026	-0.178	A_1	11.451	0.199	0.059	-0.048	-0.937
	-0.035	-0.054	-0.035	-0.042	0.010	-0.107	A_2	14.993	0.200	0.082	-0.011	6.751
	0.029	-0.064	-0.011	-0.005	0.008	-0.127	A_3	14.431	0.200	0.063	0.152	-3.500
<i>tll</i>	-0.071	-0.076	-0.063	-0.089	-0.041	0.000	A_1	13.235	0.197	0.080	-0.110	13.065
	0.096	0.019	0.044	0.036	-0.099	0.048	A_2	14.992	0.195	0.061	-0.070	-15.781
	0.191	0.059	-0.037	0.092	-0.001	0.085	A_3	14.991	0.187	0.057	-0.026	-30.979

To estimate the embryo-to-embryo variability numerically, the following relative root-mean-square (rms) deviation of individual concentrations from the average was calculated for each protein and time moment in each fixed embryo:

$$\sigma_{\text{rms}} = \sqrt{\frac{1}{|\Omega|} \int_{\Omega} \left(\frac{v_{\text{mean}}(x) - v(x)}{v_{\text{mean}}(x)} \right)^2 dx}, \quad (3)$$

where $v(x)$ is the protein concentration function in the embryo, $v_{\text{mean}}(x)$ is the embryos-averaged concentration function, x is the coordinate along the A–P axis of the embryo, Ω is the domain in the A–P axis, and $|\Omega|$ is the length of this domain. Figure 2c shows the embryos-averaged value of σ_{rms} for *Kr* as a function of time class. It is evident that the embryo-to-embryo variability is essentially reduced during cycles 12–14 A, i.e. the concentration “trajectories” from different embryos are canalized into a common stable pattern by the end of 14 A.

An additional argument in favor of quasistationarity is the known effect of positional error filtration in the gap gene expression [16]. This effect describes the reduction with time of embryo-to-embryo variability of spatial expression domain borders. For example, let us define the right border of the expression domain for gene *Kr* as the most P-proximal point at the A–P axis at which the *Kr* protein concentration takes its half-maximal value. Analysis of the same data as in Fig. 2 yields

the following values of the border standard deviation in the sample of several embryos: 1.6% of the A–P axis length in the beginning of cycle 14 A and 0.6% in the end.

MODELING RESULTS

We have found three sets of parameter values, shown in Table 1 (see also Appendix), that provide good correspondence between solutions and data; the models with these parameter values are denoted as A_1 , A_2 , and A_3 . The solution graphs in A_2 are shown in Fig. 3 in comparison with the data at three time moments. Solutions in A_1 and A_3 have similar graphs. It is seen that the models approximate the experimental data dynamics with good precision. The correspondence between the solutions and the data takes place not only in the end of cycle 14 A, but also at the intermediate moments of embryo development.

Below we compare the stability properties of solutions in models A_1 – A_3 with those in seven best variants of the initial model [9, 10], obtained by optimization of parameter values in (1) without the requirement of asymptotic stability at gastrulation. We denote these models as B_1 – B_7 .

Table 2 lists the resulting values F_0 of functional (2) after optimization in models A_1 – A_3 and B_1 – B_7 . In the models with fitting to attractor they are slightly larger than in models B_j . However, the difference is not great

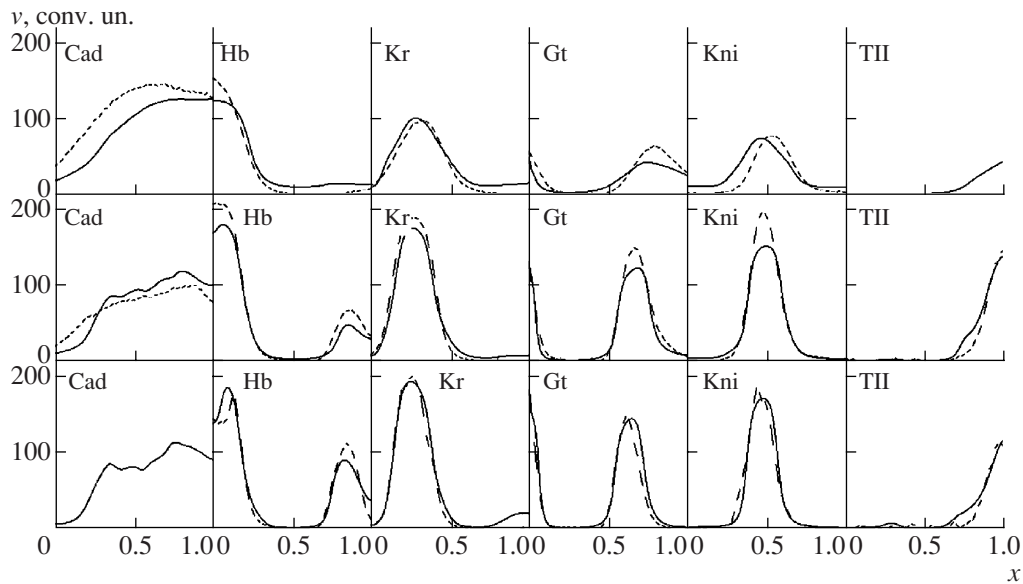


Fig. 3. The solutions in model A_2 (solid curves) in comparison with the data (dashed curves) at the following three time moments: the early cycle 14 A ($t = 24.225$ min; upper row of panels), the mid cycle 14 A ($t = 42.975$ min; middle row), and the late cycle 14 A ($t = 67.975$ min; lower row). The abscissa axis shows the dimensionless spatial coordinate x parameterizing the nucleus i position in the A–P axis domain under consideration (35–92% of the axis length). The ordinate gives the protein concentrations v (in conventional units) corresponding to the labels on the panels. The data for Tll in the early cycle 14 A and for Cad in the late cycle have not been used in constructing models A_1 – A_3 ; therefore, these graphs are absent from the corresponding panels.

and is not related to any defects in the solutions, as evident, e.g., from Fig. 3.

The proximity of solutions at the end of cycle 14 A to actual attractors can be visually estimated in Fig. 4. The solutions at $t = \tau$ are very close to the attractors in all three A models, which means that the solutions at gastrulation are asymptotically stable with $t \rightarrow \infty$. The concentration curves for proteins Hb, Gt, and Tll in A_1 from the moment $t = \tau$ are less close to the attractor than for other proteins, while A_2 and A_3 provide much the same proximity for all genes.

The asymptotic stability of solutions at $t = \tau$ can be numerically characterized, for example, by their rms deviations from the attractors:

$$E = \sqrt{\frac{1}{MN} \sum_{a,i} (v_i^a(\tau) - (v_i^a)_{\text{attr}})^2}, \quad (4)$$

where $(v_i^a)_{\text{attr}} = \lim_{t \rightarrow \infty} v_i^a(t)$ is the stationary attractor. The summation is performed over all genes and nuclei, and the sum is divided by the total number MN of terms

therein. The proximity of solutions at gastrulation to attractors in A_j and B_j in terms of E is shown in Table 2. The solutions in B_2 and B_4 tend to oscillating attractors, and, strictly speaking, E is not defined in this case. However, the table contains the values for these models as well, but they have been calculated by taking values of the oscillating solutions at a fixed large time instead of $(v_i^a)_{\text{attr}}$ in (4). It follows from the table that, as expected, solutions in the model at the end of cycle 14 A are unstable and vary substantially at large times if no additional constraints have been imposed on the solution dynamics. The “worst” of our model versions (A_1) has only half the E estimated for the “best” of the initial models (B_7).

STABILITY AGAINST PERTURBATIONS IN MODELS OF TWO TYPES

In this Section we describe the stability of solutions in models A_j and B_j under perturbations of concentrations v_i^a and parameter values. We consider three kinds

Table 2. The values F_0 from (2) obtained upon optimization, and E from (4) in models A_1 – A_3 and B_1 – B_7 . Models B_2 and B_4 have oscillating attractors. The numerical solutions at $t = 10000$ have been taken as the attractors

	A_1	A_2	A_3	B_1	B_2	B_3	B_4	B_5	B_6	B_7
F_0	14.1	14.0	13.7	11.2	10.9	10.6	10.2	10.3	10.2	9.4
E	23.9	7.5	12.2	78.3	93.1	83.1	74.5	82.2	83.1	45.9

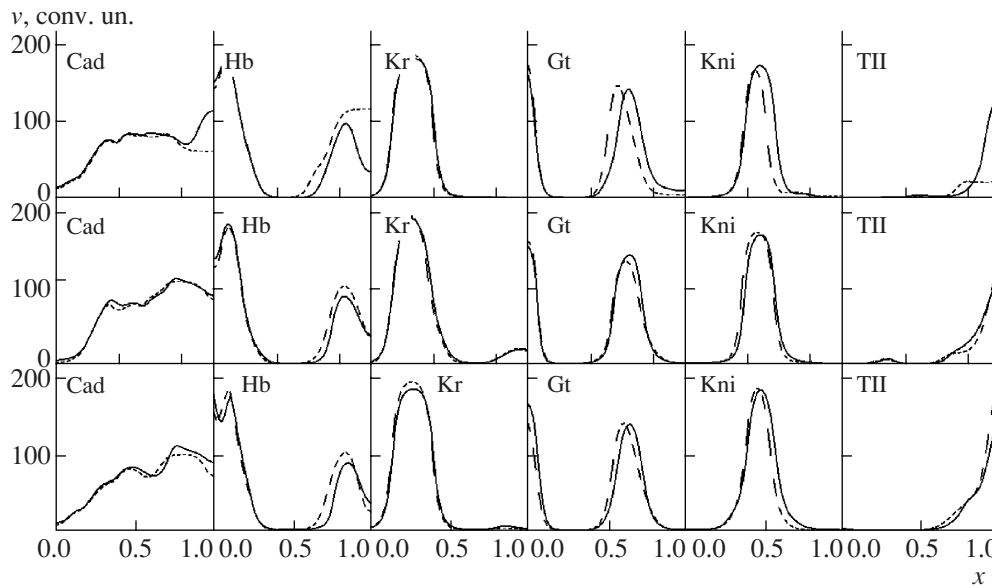


Fig. 4. The solutions in models A_1 (upper row of panels), A_2 (middle row), and A_3 (lower row) at $t = \tau$ (solid curves) in comparison with the attractors (dashed curves). The solutions in the models at $t = 10000$ min are shown as the attractors. Other notations are as in Fig. 3.

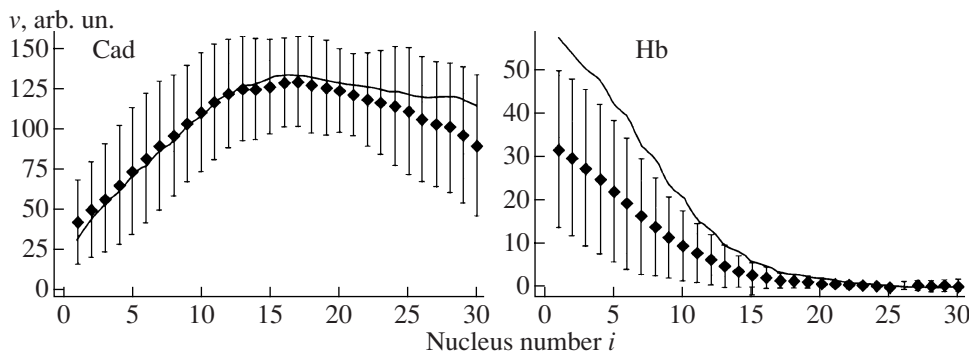


Fig. 5. The initial conditions in the model (solid curves) for Cad and Hb concentrations in comparison with the means (points) and standard deviations (error bars) in the sample of experimental concentrations of these proteins in each nucleus. The abscissa gives the nuclei numbers i in the considered spatial domain on the A-P axis in the 13th cleavage cycle. The ordinate shows the protein concentrations v_i^a in conventional units.

of perturbation, namely, the perturbations of initial conditions $v_i^a(0)$, concentrations $v_i^a(t)$ at various moments $t_k \neq 0$, and parameter values. The variation of initial conditions is supposed to model the embryo-to-embryo variability of early expression data, while the fluctuations at different positive times are related to the nucleus-to-nucleus noise taking place in each embryo.

Perturbation of Initial Conditions

The spatial curves of experimental gap gene protein concentrations scanned in various embryos (the individual curves) in the 12th cycle were used as the perturbed initial conditions [14]. That was the way the

study of stability was connected with the investigation of the embryo-to-embryo variability of early experimental data.

The data contain 15 distinct individual curves for Cad, 20 for Hb, 8 for Kr, 3 for Gt, 1 for Kni, and 14 for Tll proteins. Figure 5 shows the graphs of initial concentrations $v_i^{Cad}(0)$ and $v_i^{Hb}(0)$ in the model in comparison with the mean and its standard deviation in the sample of these experimental individual curves. It can be seen that the initial concentration profile for Cad in the model is quite close to the averaged experimental curve, while for the initial Hb concentration this is not so. The latter fact restricts the possibility of directly connecting the dynamics of variability in experimental

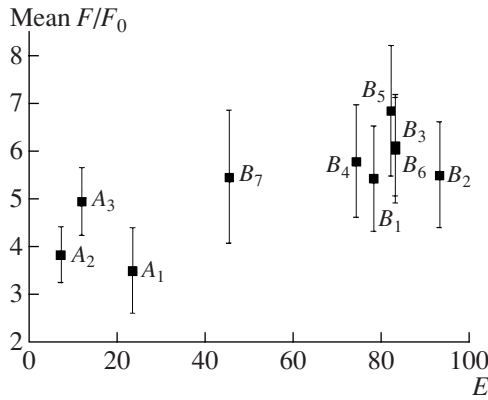


Fig. 6. The mean F/F_0 (points) and its standard deviation (error bars) in the sample of solutions with perturbed initial conditions in models A_1 – A_3 and B_1 – B_7 versus the values of E , characterizing the proximity of unperturbed solutions to attractors.

data with that in models A_j and B_j . However, we believe that comparison between the variabilities in models of the two types still makes sense, and, hence, we apply the perturbations as stated above.

Such a difference in the initial concentration $v_i^{\text{Hb}}(0)$ is a consequence of the FlyEx database development. The curve $v_i^{\text{Hb}}(0)$ in models B_j , shown in Fig. 5, has been calculated by averaging individual curves from cycle 12. However, the data added to FlyEx in the last years have shifted the average Hb concentration. We have chosen the same initial conditions in models A_j as in B_j for correct comparison between the models.

We added the model initial conditions to the present sample of individual initial curves and selected the perturbed initial conditions from this sample as follows. We took all individual curves for Cad and Hb (336 combinations); for each (Cad, Hb) pair, from the set of individual curves for the other four genes we selected five curves that were closest to the model initial conditions (5 from 1080 combinations). Therefore, from the total number of 362 880 combinations of individual experimental curves for the six genes (including the model initial conditions), we constructed 1680 sets of curves used as the perturbed initial conditions.

We calculated the functional F for each perturbed solution, characterizing the rms distance between the solution and the experimental data. As the unperturbed solutions in all models were close to the data, the scaled values F/F_0 could be used to estimate the deviation of perturbed solutions from the unperturbed ones. The mean F/F_0 with standard deviations are plotted in Fig. 6 versus E from Table 2. The figure shows the clear clusterization of mean F/F_0 in the models of the two types. Namely, these values are less than 5 in A_j and larger than 5.5 in B_j . An important point is the model B_7

position in the figure. It follows from Table 2 that E in model B_7 is significantly smaller than in the other B_j but significantly larger than in A_j . Hence, the solutions in B_7 at $t = \tau$ are close enough to an attractor to consider model B_7 as “intermediate” between A_j and the other B_j . Figure 6 demonstrates that the average deviation of perturbed solutions in B_7 also takes a position at the boundary between the two clusters.

The coefficient of correlation between the average F/F_0 and E is $r = 0.80$, and it is 0.84 when models B_2 and B_4 are discarded as having nonstationary attractors.

In order to analyze the dispersion of perturbed solutions around the mean in more details, we considered the sample of values $\{v_i^a(t_k)\}$ across all perturbed solutions v_i^a , where t_k were the time moments for which the experimental data existed ($k = 1, \dots, K$). We calculated the standard deviation in this sample for each fixed a, i , and k and then averaged these standard deviations over all genes, nuclei, and moments t_k . The resulting values for each model are shown in Fig. 7a versus E .

The same tendency can be seen as for the averages from Fig. 6. The models with quasistationary patterns at the end of cycle 14 A have smaller dispersion of solutions. The correlation coefficients corresponding to Fig. 7a are $r = 0.81$ and $r = 0.82$ with and without models B_2 and B_4 , respectively.

It should be noted that the analogous averaged standard deviation calculated in the sample of experimental individual curves at moments t_k equals 13.4. Therefore, models A_j have better stability than models B_j , but their stability still does not reach the experimentally observed one.

Perturbation of Concentrations at Various Times

The perturbations of solutions at positive time moments are supposed to model, to some extent, the nucleus-to-nucleus noise present in the individual experimental concentration curves [14]. It is known from the stochastic modeling experience that, at least in a stationary regime of gene expression, the stochastic concentration values X group around the mean X^{mean} according to the Poisson distribution law. This means that the standard deviation is proportional to the root of the mean: $\sigma \sim \sqrt{X^{\text{mean}}}$ [17]. For a given mean, we can model the stochastic variable with such a distribution in the simplest case as follows:

$$X = X^{\text{mean}} + \sqrt{X^{\text{mean}}} \varepsilon \quad (5)$$

where ε is a random variable with a normal distribution $\varepsilon \sim N(0, \sigma)$, having zero mean and fixed standard deviation σ .

Analysis of individual experimental concentration curves for various proteins from FlyEx has not revealed

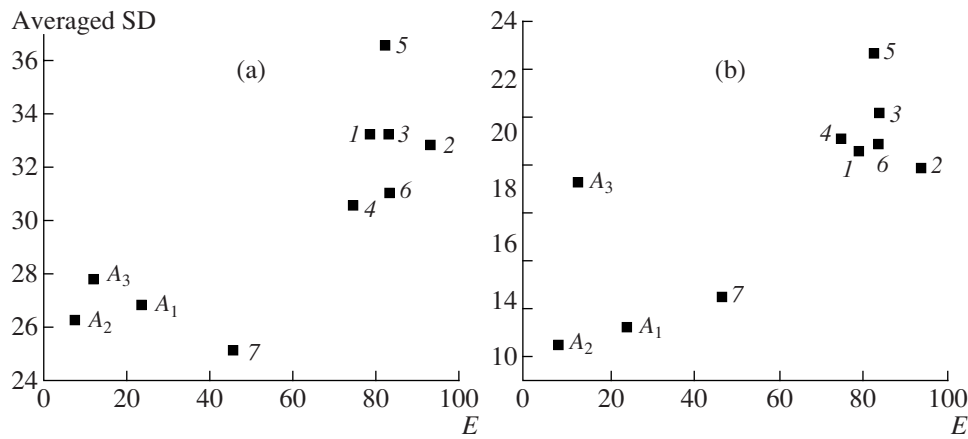


Fig. 7. The standard deviations in the sample of perturbed solutions $\{v_i^a(t_k)\}$ (where t_k are the moments for which there were data) averaged over $a, i,$ and k in models A_1 – A_3 and B_1 – B_7 versus E . The case of perturbed initial conditions is shown in (a), and the perturbations according to (6) in (b). The standard deviations in (b) have been additionally averaged over the three values of σ . Models B_1 – B_7 are labeled only by numbers for better visibility.

a clear answer about the shape of the distribution approximating the variability of v_i^a across nuclei. Some expression patterns lead to the Poisson law, while others involve the log-normal law, prescribing $\sigma \sim X^{\text{mean}}$. Some studies also indicate the presence of experimental noise in such estimates, which cannot be eliminated at the moment.

Using this information, we applied the Poisson noise in the form (5) to model the perturbations. The solution values at fixed time moments $t_s, s = 1, \dots, S$, were perturbed in the following way:

$$(v_i^a)_{\text{new}}(t_s) = v_i^a(t_s) + \sqrt{v_i^a(t_s)}\varepsilon, \quad (6)$$

where $\varepsilon \sim N(0, \sigma)$. The formula (6) coincides with (5) in which the current solution values $v_i^a(t_s)$ are taken instead of X^{mean} for simplicity. This is possible because the model equations can be interpreted as equations for averages. Hence, if a solution of these equations is perturbed at moment t_{s-1} , then it will be to some extent “restored” by moment t_s , and $v_i^a(t_s)$ will not differ much from the genuine average, of course under the assumption that t_{s-1} and t_s are sufficiently distant from each other.

The perturbations were performed each two minutes, starting from $t_1 = 2$ min and excluding moments preceding the times for which the data were available. This exclusion was done in order to reduce the influence of stochastic perturbations on the calculation of F from (2). Therefore, we had in total $S = 24$ moments t_s . The following values for σ were used: $\sigma = 0.1, \sigma = 0.5,$ and $\sigma = 1$. An analysis of individual experimental curves gave an approximate range $0.5 < \sigma < 1$ for various proteins in cycle 14 A. There were 500 random per-

turbations performed according to (6) in each model at each moment t_s and for each σ .

The mean F/F_0 with standard deviations calculated in the samples of perturbed solutions with given σ values are plotted in Fig. 8 versus E from Table 2. The results indicate that the correlation between the model stability to perturbations and the quasistationarity of solutions at gastrulation presented in Fig. 6 and 7a persists when the perturbations are spread along the time interval. The correlation coefficients corresponding to Fig. 8 are $r = 0.81$ at $\sigma = 0.1, r = 0.90$ ($\sigma = 0.5$), and $r = 0.76$ ($\sigma = 1$). The coefficients r have similar values when models B_2 and B_4 are discarded.

Some nonlinear effects in the behavior of perturbed solutions under increased noise can be seen in Fig. 8. Model B_7 at small noise has maximal F/F_0 , which means that in this case the model cannot be considered as intermediate between the two types. The large dispersion for B_7 indicates that even small perturbations may lead to relatively large deviations of solutions from the experimental data. At larger σ values, the place of B_7 changes according to the intermediate model status. On the other hand, it is seen that solutions in A_3 behave similarly to those in the other A_j at small noise, but at $\sigma = 1$ the mean F/F_0 in this model essentially increases, and A_3 takes the boundary position between A_j and B_j . Visual inspection of perturbed solutions in A_3 suggests that such behavior is mostly related with the instability of the Kr and Gt patterns in the model at $\sigma = 1$.

The behavior of perturbed solutions is exemplified in Fig. 9 for Kr in models A_2 and B_3 . It is seen that the Kr left border in B_3 becomes unstable already at small perturbations, while the right border does not appreciably change under noise. The larger perturbation amplitudes lead to pronounced deformation of the Kr pattern

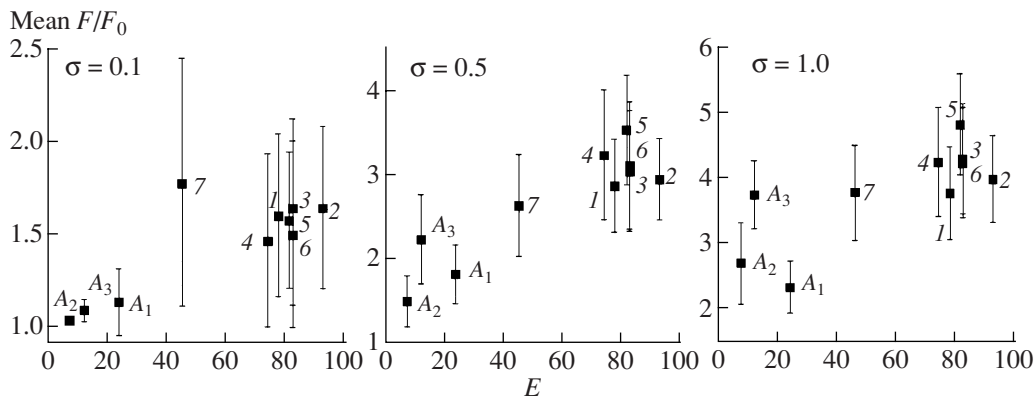


Fig. 8. Same as in Fig. 6 but for the sample of solutions perturbed according to (6), at the three values of σ . Models B_1 – B_7 are labeled only by numbers for better visibility.

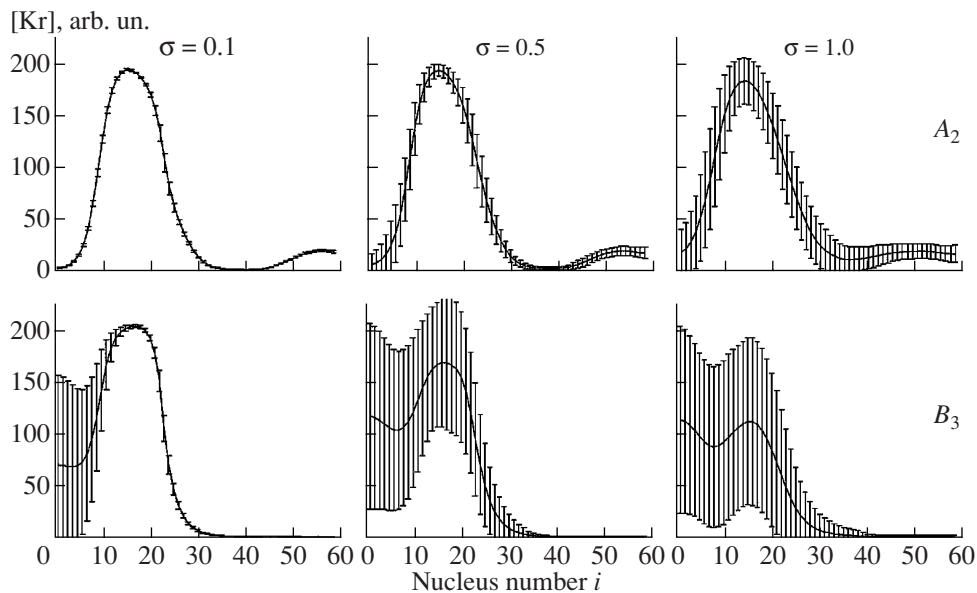


Fig. 9. The mean Kr concentration (curves) and the standard deviation (error bars) in the sample of solutions perturbed according to (6) in models A_2 (upper row of panels) and B_3 (lower row) at given σ and $t = 67.975$ min.

in B_3 . The Kr pattern in A_2 keeps its shape at all σ values, and only the dispersion around the mean pattern increases.

Figure 7b presents the standard deviations of perturbed solutions averaged over all nuclei, genes, data times, and σ values. The coefficient of correlation between this measure of spread and E is in this case $r = 0.77$ (0.79 without B_2 and B_4). The figure also shows the effect of model A_3 shift described above.

Perturbation of Parameter Values

The perturbations of parameter values in the model equations could be associated with the environmental noise. We did not have any specific information about the possible general distribution for such noise, and,

therefore, we applied the normal distribution. Again, it was difficult to choose a unified amplitude for perturbations of different parameters. We performed normally distributed random perturbations of parameter values in models A_j and B_j with standard deviations σ equal to 1, 5, and 10% of the unperturbed parameter values. Denoting the parameter vector as $q = \{R^a, D^a, \lambda^a, T^{ab}, m^a, h^a\}$ with components q^s , the perturbation scheme had the form

$$q_{\text{new}}^s = q^s + |q^s| \varepsilon, \quad \varepsilon \sim N(0, \sigma), \quad (7)$$

$$\sigma \in \{0.01; 0.05; 0.1\}.$$

There were 500 random perturbations performed according to (7) in each model and for each σ value.

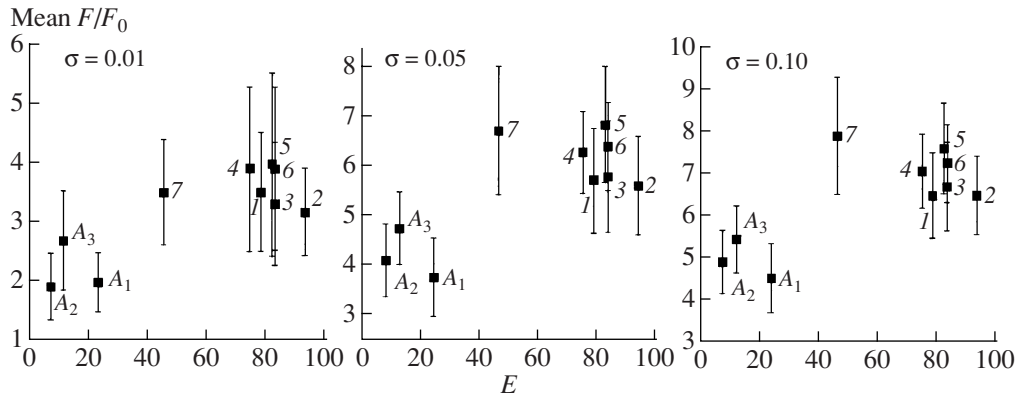


Fig. 10. Same as in Fig. 6 but for the sample of solutions in models A_j and B_j with the parameters perturbed according to (7) at given values of σ . Models B_1 – B_7 are labeled only by numbers for better visibility.

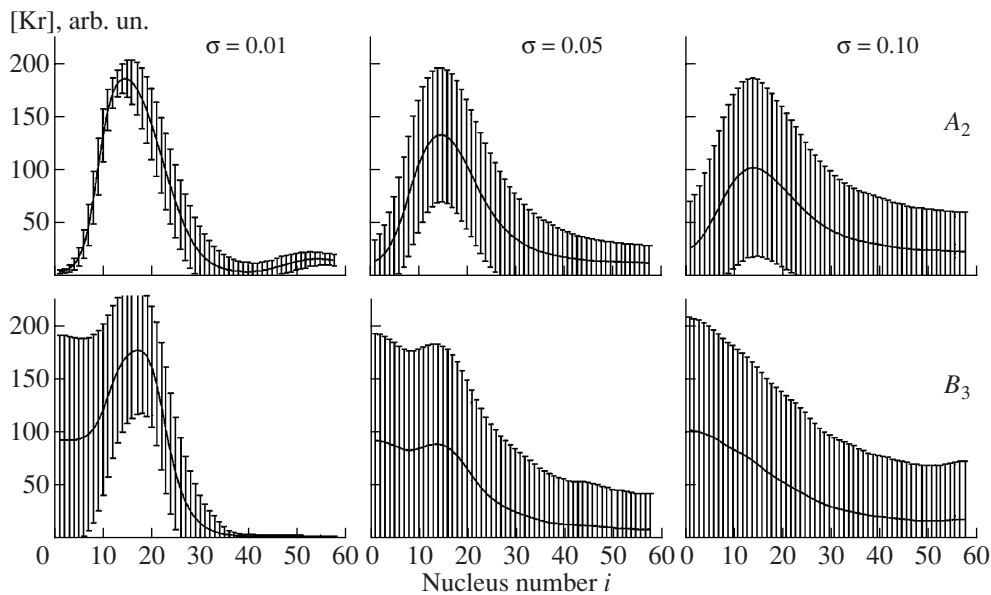


Fig. 11. Same as in Fig. 9 but for the sample of solutions in models A_2 and B_3 with the parameters perturbed according to (7) at given values of σ .

The results are presented in Fig. 10 in terms of F/F_0 . The correlation coefficients for mean F/F_0 and E are $r = 0.81$ ($\sigma = 0.01$), $r = 0.74$ ($\sigma = 0.05$), and $r = 0.71$ ($\sigma = 0.1$). One can see that the correlation weakens as σ grows, in particular, because of the rising instability of model B_7 , which has the maximal F/F_0 at $\sigma = 0.1$.

Noteworthy is the marked sensitivity of all models to variation of the parameter values. It follows from Fig. 10 that perturbation of all parameters even at $\sigma = 0.01$ increases the rms deviation of solutions from the data by a factor of 2–2.5 in models A_j and 3–4 in models B_j .

The behavior of the Kr concentration at various perturbation amplitudes is shown in Fig. 11. Even at the high solution variability, the mean concentration profile in A_2 preserves a relatively correct shape until $\sigma = 0.1$.

At the same time, the left border of the Kr expression domain in B_3 is almost destroyed at $\sigma = 0.05$.

We have also performed type (7) perturbations, but only for parameters from two classes, $q = \{R^a, D^a, \lambda^a\}$ and $q = \{T^{ab}, m^a, h^a\}$. Two examples are shown in Fig. 12 of how the mean F/F_0 varies when the perturbation amplitude is raised in models A_2 and B_3 . The curves corresponding to perturbations of all parameters and of $\{T^{ab}, m^a, h^a\}$ almost coincide. Therefore, this parameter class is most sensitive to the perturbations. On the other hand, perturbations of $\{R^a, D^a, \lambda^a\}$ influence the solutions considerably less. It follows from the figure that, for example, solutions in A_2 are absolutely stable in the 1% vicinity of parameter values in this class. This is not true for B_3 .

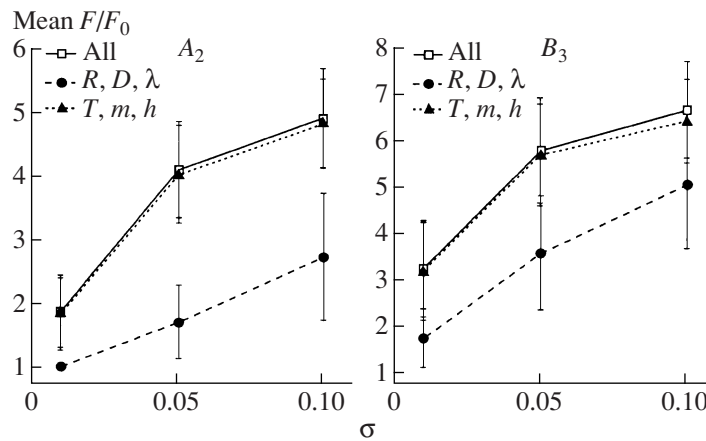


Fig. 12. The mean F/F_0 (dots) and the standard deviation (error bars) in the sample of solutions in models A_2 and B_3 with perturbed parameter values at various σ . The three curves for each model correspond to the parameter classes specified on the figure.

CONCLUSIONS

The results described here imply that the considered model of segmentation gene expression allows the quasistationary behavior of solutions at the end of cycle 14 A. This particularly means that the reduction of embryo-to-embryo variability in the expression patterns occurring by the onset of gastrulation (Fig. 2) indeed can be mathematically interpreted as the canalization of trajectories with different initial conditions and external factors to a single attractor. The results on stability indicate that the model with a quasistationary solution at gastrulation has better stability against noise of various nature.

An obvious “biological function” of such an attractor in the operation of the gap gene system is to provide a more precise and less variable positioning of the expression patterns under the inevitable variations of the embryo development conditions. This precision is especially important because the gap genes are just one step in the segmentation gene cascade, and their expression patterns determine the expression in the pair-rule gene system. Therefore, error filtration in the pattern positioning inside the cascade has a clear goal and must be equipped with appropriate mechanisms. We believe that the quasistationarity provides one of these mechanisms.

On the other hand, such an intermediate role played by the gap genes in the *Drosophila* early development hides, up to some extent, the necessity for the patterns at gastrulation to be close to the attractor. Indeed, only the bounded time interval $0 \leq t \leq \tau$ is biologically meaningful in models B_j and A_j , and the dynamics only in this time controls the basic properties of the pair-rule gene expression. However, model (1) describes, in a sense, the dynamics of average concentrations and does not take into account the inevitable variation in solutions. For a single solution of equations (1) at fixed parameter values, there is no need in the asymptotic stability of the $t = \tau$ solution at large times. The fact that the solution in

B_j significantly varies at times $t > \tau$ does not mean much for the analysis of this “average” solution at $t < \tau$. But this property of model B_j leads to a large dispersion of solutions under the variation of concentration and parameter values occurring in reality. In this context, the model dynamics at times $t > \tau$ becomes important for correct model behavior at times $0 \leq t \leq \tau$. We must emphasize that the times $t > \tau$ should not be related to the corresponding physical time moments, but are considered only in the mathematical model.

Comparing the stability against various perturbations in B_j and A_j , we conclude that these results support the hypothesis that the proximity to attractor is necessary for more precise expression pattern positioning and, hence, for more robust “signal” transmission over the segmentation gene cascade. The study of all perturbation types (initial conditions, concentrations at times $t > 0$, and parameter values) has revealed a strong correlation between the quality of perturbed solutions, defined by their similarity to the experimental data, and the stationarity rate at times $t > \tau$ ($0.71 \leq r \leq 0.90$ depending on the situation). Models A_1 – A_3 exhibit more stable dynamics at times $0 \leq t \leq \tau$ than models B_1 – B_7 .

Model B_7 has played an important role in estimating the correlation. This model occupies an intermediate position between A_j and other B_j by the proximity of the solution at gastrulation to the attractor. This intermediate nature of B_7 is largely preserved in the solution response to perturbations.

Finally, we should note that, despite the improved stability of A_j , models of both types exhibit substantial spreading of solutions under perturbation of initial conditions and parameter values. This is partly explained by the distributions chosen for the perturbations. In the initial conditions case, for example, the mean experimental Hb concentration curve in the 12th cycle differs significantly from the initial condition for v_i^{Hb} in the

Table 3. The comparison of topologies in the subnetwork of gap genes *hb*, *Kr*, *gt*, and *kni* in models B_6 and A_1 – A_3 . The *bcd* column corresponds to parameters m^a , and other columns to parameters T^{ab} . The signs in the table describe the type of action exerted by genes indicated in column heads on genes specified at the left; (+) means activation in a corresponding model, (–) repression, and (0) lack of interaction (see text for details). The upper entry inside each square corresponds to model B_6 , and the lower entries to models A_1 – A_3 as outlined in the rightmost column. For example, it follows from the square at the intersection of the *cad* column and the *hb* row that *hb* is activated by *cad* in models B_6 and A_3 , repressed in A_2 , and interaction is negligible in A_1

	<i>bcd</i>	<i>cad</i>	<i>hb</i>	<i>Kr</i>	<i>gt</i>	<i>kni</i>	<i>tll</i>	
<i>hb</i>	+	+	+	0	+	–	0	B_6
	+ / + / +	0 / – / +	– / – / 0	– / – / 0	– / – / –	– / – / –	– / – / 0	$A_1 / A_2 / A_3$
<i>Kr</i>	+	+	–	+	–	–	–	B_6
	+ / – / +	+ / – / +	– / – / 0	– / – / –	– / – / –	– / – / –	– / – / –	$A_1 / A_2 / A_3$
<i>gt</i>	+	+	–	–	+	0	–	B_6
	+ / + / –	+ / + / +	– / + / +	– / – / –	0 / + / +	– / + / 0	– / – / –	$A_1 / A_2 / A_3$
<i>kni</i>	+	+	–	–	–	+	–	B_6
	– / – / +	+ / – / +	– / – / –	– / – / –	– / – / –	+ / + / +	– / – / –	$A_1 / A_2 / A_3$

models (Fig. 5). To some extent, however, such behavior of perturbed solutions is an intrinsic property of the model itself. Therefore, the use of attractors and their basins of attraction is an important but not the final step on the way of constructing a robust model of the gap gene expression dynamics.

APPENDIX

COMPARISON OF PARAMETERS IN MODELS OF TWO TYPES

Table 1 contains the parameter values in models A_1 – A_3 . The diffusion coefficients D^a in the table correspond to the values in cycle 14 A.

The parameter optimization in A_3 differed from that in A_1 and A_2 in two aspects. First, the experimental data for Tll was not used in A_3 for fitting at times $t > \tau$. Second, values $h_2 = h_4 = h_5 = -3.5$ were fixed during optimization in A_3 (see Table 1).

The parameter values from Table 1 are similar to those from models B_j in the order of magnitude. The topology of gap gene interactions predicted by the models is of special interest. The four genes *hb*, *Kr*, *gt*, and *kni* are usually discussed in this context [10]. In Table 3 we compare the signs of interaction of these genes with each other and with *cad*, *tll*, and *bcd* in models A_j and B_6 . We compare A_j with B_6 because, according to [10], B_6 is the most representative among all B_j in terms of the gene interaction topology. Following [10], we use the threshold value 0.005 to define the interaction sign. Namely, we assume that gene *b* represses gene *a* if $T^{ab} \leq -0.005$ (“–” sign in Table 3), activates it if $T^{ab} \geq 0.005$ (“+”), and there is practically no interaction if $-0.005 < T^{ab} < 0.005$ (“0”). This threshold value

is chosen empirically, i.e., selected by numerical analysis of model solutions.

It follows from the table that model B_6 estimates the influence of maternal genes *bcd* and *cad* as activation, while these interactions can be repressive for some genes in some A_j . In this aspect, model B_6 is most similar to A_3 , in which *bcd* represses only *gt*.

Based on the analysis of this subnetwork topology, the authors of [9, 10] have concluded that the subnetwork genes exhibit weak self-activation and mutual repression. The same conclusion is valid in models A_j with some exceptions. The main difference from model B_6 is provided by the *hb* self-regulation and the regulation of *gt* by *hb*. At the same time, the topology in B_j also does not fully satisfy the above conclusion, as *gt* activates *hb* in these models. All models A_j estimate this interaction as repression.

ACKNOWLEDGMENTS

The authors thank M.G. Samsonova, E.M. Myasnikova, and S.Yu. Surkova for discussions.

The work was supported by NIH grant RR07801, CRDF GAP award RUB1-1578, and RFBR-NWO grant 047.011.2004.013.

REFERENCES

1. P. A. Lawrence, *The Making of a Fly* (Blackwell Sci. Publ., Oxford, UK, 1992).
2. I. F. Zhimulev, *Soros. Obraz. Zh.* no. 7, 30 (1998).
3. M. Akam, *Development* **101**, 1 (1987).
4. P. W. Ingham, *Nature* **335**, 25 (1988).
5. J. Reinitz and D. H. Sharp, *Mech. Dev.* **49**, 133 (1995).

6. L. Sánchez and D. Thieffry, *J. Theor. Biol.* **211**, 115 (2001).
7. R. N. Tchuraev and A. V. Galimzyanov, *Mol. Biol.* **35**, 933 (2001).
8. V. V. Gursky, J. Jaeger, K. N. Kozlov, et al., *Physica D* **197**, 286 (2004).
9. J. Jaeger, S. Surkova, M. Blagov, et al., *Nature* **430**, 368 (2004).
10. J. Jaeger, M. Blagov, D. Kosman, et al., *Genetics* **167**, 1721 (2004).
11. H. Kitano, *Nature Rev. Genet.* **5**, 826 (2004).
12. E. Mjolsness, D. H. Sharp, and J. Reinitz, *J. Theor. Biol.* **152**, 429 (1991).
13. E. Myasnikova, A. Samsonova, K. Kozlov, et al., *Bioinformatics* **17**, 3 (2001).
14. FlyEx database: <http://urchin.spbcas.ru/flyex>; FlyEx database (mirror): <http://flyex.ams.sunysb.edu/FlyEx>.
15. K. W. Chu, Y. Deng, and J. Reinitz, *J. Comput. Phys.* **148**, 646 (1999).
16. S. Surkova, M. Samsonova, D. Kosman, et al., *Dev. Biol.* **313**, 844 (2008).
17. M. Kaern, T. C. Elston, W. J. Blake, and J. J. Collins, *Nature Rev. Genet.* **6**, 451 (2005).
18. Manu, S. Surkova, A. Spirov, V. V. Gursky, et al., Canalization in the *Drosophila* blastoderm (submitted).

Reproduced with permission of the copyright owner. Further reproduction prohibited without permission.